

Vibration System Analysis of Magnetic Journal Bearing for MMR Condition

Dokyu Kim^a, SeungJoon Baik^b, Jeong Ik Lee^{a*}

^aDepartment of Nuclear and Quantum Engineering, KAIST, Daejeon, South Korea

^bKorea Atomic Energy Research Institute, Daejeon, South Korea

Corresponding author : jeongiklee@kaist.ac.kr

1. Introduction

The attention on the distributed power generation with nuclear energy is increasing due to the electricity grid decentralization and demand for mobile power generation without emission of CO₂. A concept of fully modularized fast reactor with a supercritical CO₂ (S-CO₂) cooled direct Brayton cycle, namely KAIST Micro Modular Reactor (MMR), for 10 MWe power output is being developed for the distributed power generation with the nuclear energy. Furthermore, MMR can be applied to marine propulsion. This is to substitute a diesel engine to meet newly released International Maritime Organization (IMO) regulation on greenhouse gas emission [1].

In the proposed MMR, an appropriate bearing technology to levitate the shaft in the turbomachinery is required. It should be designed to be hermetic so that lubrication fluid is not necessary because it forces to add oil supply and sealing sub-system that complicates the system [2,3]. There are two types of hermetic type bearing: (1) gas bearing and (2) magnetic bearing. Gas bearing does not have enough load to support MMR turbomachinery condition. Therefore, magnetic bearing is a proper choice as supported by the previous research [4] and Fig. 1.

TM Feature	Power (MWe)					
	0.3	1.0	3.0	10	30	100
Bearings	Gas Foil		Hydrodynamic oil			
	Magnetic			Hydrostatic		

Fig. 1. Bearing options for S-CO₂ Brayton Cycles for various power scales [4]

However, an instability issue with magnetic bearing levitation was repeatedly mentioned under S-CO₂ high speed operating conditions. Due to this instability, the shaft eccentricity can grow until the clearance disappears leading to rotor and stator contact. Shaft orbit regarding this issue is shown in Fig. 2. On the other hand, much higher speed operating in air condition does not have the same issue as shown in Fig. 3.

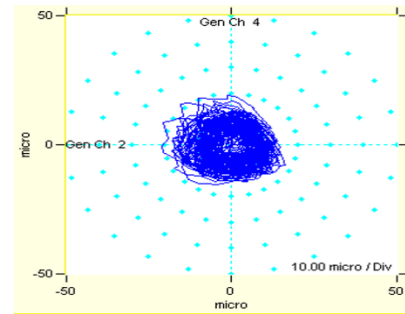


Fig. 2. Shaft center orbit at 14,000rpm, 43°C, 78 bar under S-CO₂ condition

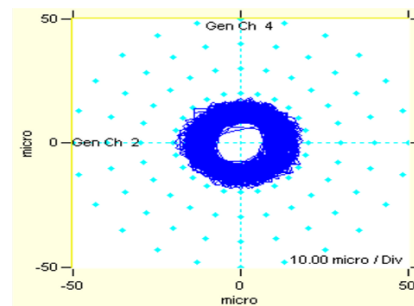


Fig. 3. Shaft center orbit at 30,000rpm under air condition

In this paper, the modeled S-CO₂ lubrication pressure distribution in the magnetic journal bearing geometry with uniform circular motion is analyzed with its physical properties. To verify the model results, the shaft trajectory data from the experiments is analyzed to obtain the net & lubrication force. The forces are compared with the model results from shaft trajectory input. To understand various forces measured from the experiments, the results are analyzed with Fast Fourier Transform (FFT) method and 2nd order fitting. The instability is discussed in terms of the state space and force distribution.

2. Methods and Results

2.1 Flow induced force on shaft

An Active-control Magnetic Bearing (AMB) levitates a rotating shaft with electromagnets with magnetic force. The force from an electromagnet is expressed as in eq. (1). The AMB's 8 electromagnets are located as shown in Fig. 4. The empty space in Fig. 4 is filled with the working fluid. The fluid can generate vortices and it can destabilize the shaft.

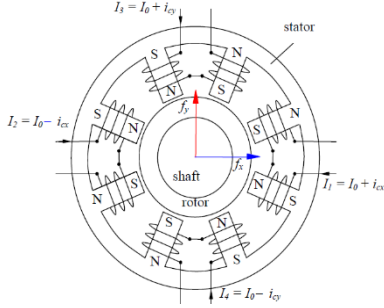


Fig. 4. Electromagnets in the magnetic bearing [5]

$$f = \frac{B^2 A_g}{2\mu_0} = \frac{\mu^2 N^2 I^2 A_g}{2\mu_0 l_g^2} \quad (1), [5]$$

The fluid force is caused by pressure distribution around the shaft. In this case, Reynolds equation is the governing equation to describe the interaction. It is derived by substituting the velocity profile from Navier-Stokes equation to the continuity equation for thin film [6]. The geometry where this equation is applied is described in Fig. 5.

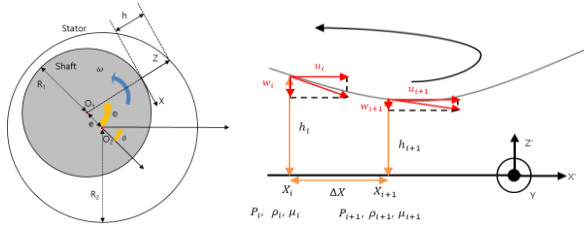


Fig. 5. Coordinate description of Reynolds equation with geometry of the unbalanced shaft and the stator

In this research, the axial direction force is assumed to be negligible because v is relatively smaller than u . Therefore, the governing equation can be simplified as in eq. (2) with turbulence model which is described in Table I [7]. Before solving this equation, the transient term in right hand side (RHS) is approximated by assuming uniform circular motion of the shaft center. This is numerically solved with finite difference method (FDM).

$$\frac{\partial}{\partial x} \left(\frac{\rho h^3}{k_x \mu} \frac{\partial p}{\partial x} \right) = \left(\frac{hu}{2} \right) \frac{\partial \rho}{\partial x} + \left(\frac{u}{2} \frac{\partial h}{\partial x} \right) \rho + \frac{\partial(\rho h)}{\partial t} \quad (2)$$

($k_x = 12 + K_x Re^{n_x}$, Re : Reynolds number)

Table I. Coefficient in Ng-Pan model

Reynolds number, Re	K_x	n_x
$50,000 < Re$	0.0388	0.8
$5000 < Re < 50000$	0.0250	0.84
$Re < 5000$	0.0039	1.06

The analyzed range is summarized in Table II. The modeling results are shown with the fluid force for various thermal properties in Figs. 6 and 7.

Table II. Operation condition range of the model

Supply temperature	10 ~ 50 °C
Supply pressure	50 ~ 100bar
Rotational speed	30000 RPM
Eccentricity ratio, $\epsilon = e/(R_2 - R_1)$	0.07

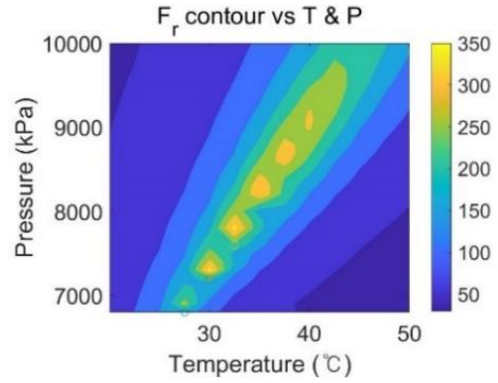


Fig. 6. F_r contour, 30000RPM, $\epsilon=0.07$

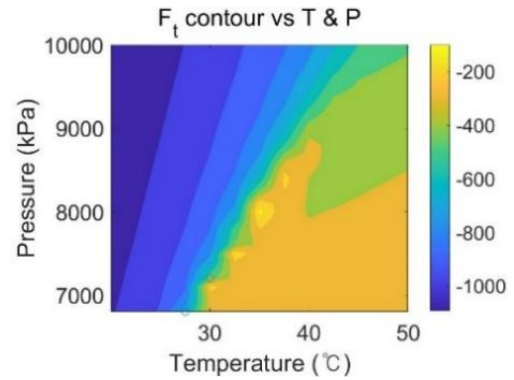


Fig. 7. F_t contour, 30000RPM, $\epsilon=0.07$

Based on eq. (2), the results show that the instability phenomena are based on the density change or high density itself. Therefore, the analysis for air condition with high density & pressure is also evaluated for the comparison. The first term of the RHS, $\left(\frac{hu}{2}\right) \frac{\partial \rho}{\partial x}$ around the shaft is plotted in Fig. 8 and the second term, $\left(\frac{u}{2} \frac{\partial h}{\partial x}\right) \rho$ is shown in Fig. 9. The last term, $\frac{\partial(\rho h)}{\partial t}$ is plotted in Fig. 10. From these figures, it is concluded that the significant difference between the high density air and the S-CO₂ condition is caused by the spatial change of the density. The forces calculated from this distribution is organized as Table III. From Table III, it is concluded that the density changes induce F_r to become larger. This also explains the tendencies from Fig. 6

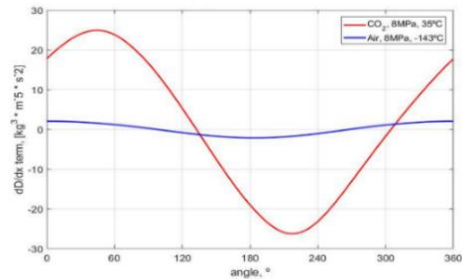


Fig. 8. $\left(\frac{hu}{2}\right) \frac{\partial \rho}{\partial x}$ around the shaft, $\epsilon = 0.25$ and 30,000 RPM

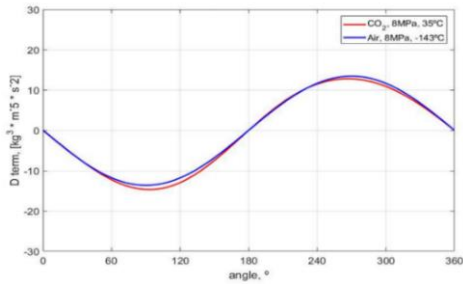


Fig. 9. $\left(\frac{u}{2} \frac{\partial h}{\partial x}\right) \rho$ around the shaft, $\epsilon = 0.25$ and 30,000 RPM

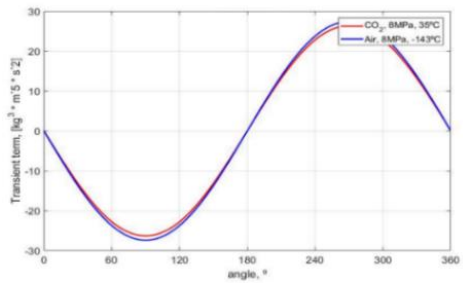


Fig. 10. $\frac{\partial(\rho h)}{\partial t}$ around the shaft, $\epsilon = 0.25$ and 30,000 RPM

Table III. Force on the shaft, $\epsilon = 0.25$ and 30,000 RPM

Thermal condition	F_x (N)	F_z (N)
Air at 8 MPa, -143 °C	35.3	-1433.6
CO ₂ at 8 MPa, 35 °C	265.2	-1344.7

2.2 Experimental analysis of magnetic bearing instability

During the experiment, the CO₂'s thermal state is controlled by S-CO₂ pressurizing experiment (S-CO₂PE) facility. The AMB test rig is attached to this facility as shown in Fig. 11. The AMB test rig consists of the compressor and the AMB. The impeller is removed so only the bearing effect is expected to be dominant.

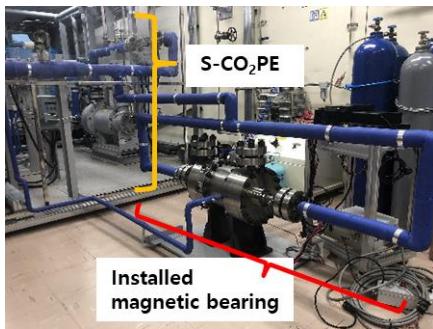


Fig. 11. The AMB & compressor system for S-CO₂

The tests are proceeded for different RPM under 8 MPa & 36 °C (350kg/m³) conditions. The shaft trajectory is shown in Fig. 12. It is observed that the shaft motion does not keep single revolving center when the RPM increases.

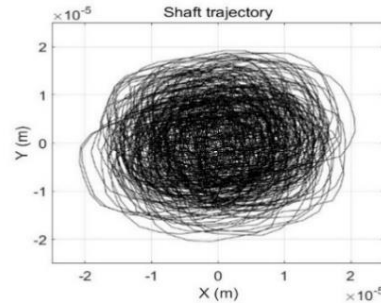


Fig. 12. Shaft trajectory data from S-CO₂ test and 30,000 RPM

The difference of the shaft trajectory from air test and S-CO₂ test is analyzed with Fast Fourier Transform (FFT). The FFT waterfall plot is shown in Fig. 13 for air test and Fig. 14 for S-CO₂ test.

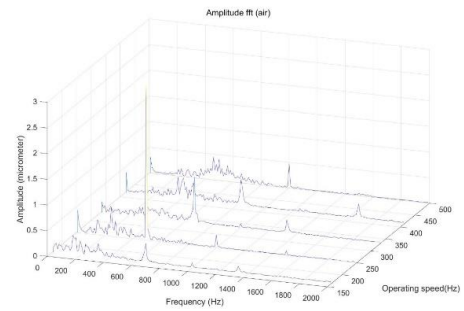


Fig. 13. FFT of the shaft trajectory data from air test

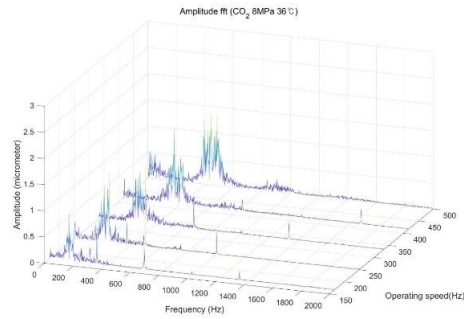


Fig. 14. FFT of the shaft trajectory data from S-CO₂ test

The difference of FFT between air and S-CO₂ test is significant in frequency range lower than operation speed. The noise in this range grows when the fluid whirl appears. To analyze the S-CO₂ effect, fluid force from experiments is calculated as shown in Fig. 15.

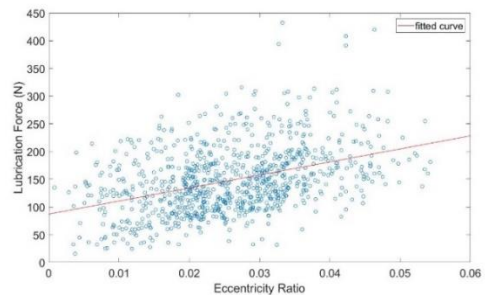


Fig. 15. F_{LUB} with 30,000 RPM

From this relationship, the stiffness is $6.47 \text{ N}/\mu\text{m}$ but it seems that F_{LUB} has weak relationship with ϵ . To explain this, other factor influences to the F_{LUB} should be found. For this goal, the net force is fitted with shaft position and velocity as shown in Fig. 16 and eqs. (3) to (5) [9].

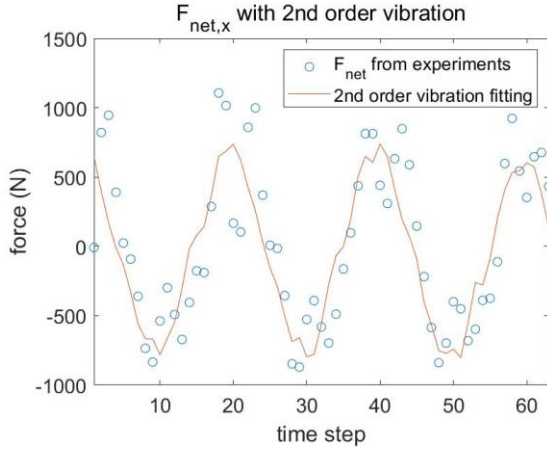


Fig. 16. 2nd order system fitting of the $F_{net,x}$

$$\dot{X} = AX + Bu \quad (3)$$

$$X = \begin{pmatrix} \dot{x} \\ \dot{y} \\ x \\ y \end{pmatrix} \quad (4)$$

$$A = \begin{pmatrix} -\frac{c_{xx}}{m} & -\frac{c_{xy}}{m} & -\frac{K_{xx}}{m} & -\frac{K_{xy}}{m} \\ -\frac{c_{yx}}{m} & -\frac{c_{yy}}{m} & -\frac{K_{yx}}{m} & -\frac{K_{yy}}{m} \\ 1 & 0 & 0 & 0 \\ 0 & 1 & 0 & 0 \end{pmatrix} \quad (5)$$

From Fig. 16, It is shown that the 2nd order system can explain the relationship between the shaft net force and the shaft trajectory. This 2nd order system fitting is planned to be analyzed with control theory.

3. Summary and Conclusions

From the developed lubrication model, it is concluded that the instability of the magnetic bearing control can be caused by S-CO₂'s physical properties. Based on this results, a magnetic bearing experimental facility is constructed. Tests for various RPMs were performed for verifying the model and the instability sources. The comparison between the model and the tests shows that the spatial change of the fluid density could cause the instability.

The test results with shaft trajectory is analyzed with frequency domain and the forces exerted to the shaft is obtained and compared with model results. This shows significant difference between air and S-CO₂ condition. Obtained forces are considered as a 2nd order vibration system. This is planned to be analyzed with control theory. Furthermore, the magnetic bearing's stiffness and damping coefficient will be analyzed for transient model. With this, dynamics of the shaft can be established for

several different conditions. Well validated model can be adapted to MMR with transient operation. After developing an accurate model, the control logic of the magnetic bearing can be finally suggested.

REFERENCES

- [1] Kim, S. G., Yu, H., Moon, J., Baik, S., Kim, Y., Jeong, Y. H., and Lee, J. I. (2017) A concept design of supercritical CO₂ cooled SMR operating at isolated microgrid region. *Int. J. Energy Res.*, 41: 512–525. doi: 10.1002/er.3633.
- [2] Tsuji, Tomoya, et al. "Solubility and Liquid Density Measurement for CO₂+ Lubricant at High Pressures." *Asian Pacific Confederation of Chemical Engineering congress program and abstracts Asian Pacific Confederation of Chemical Engineers congress program and abstracts.* The Society of Chemical Engineers, Japan, 2004.
- [3] Seeton, Christopher J., and Predrag Hrnjak. "Thermophysical properties of CO₂-lubricant mixtures and their affect on 2-phase flow in small channels (less than 1mm)." (2006).
- [4] Siemicki, James J., et al. "Scale dependencies of supercritical carbon dioxide Brayton cycle technologies and the optimal size for a next-step supercritical CO₂ cycle demonstration." *SCO₂ power cycle symposium.* 2011.
- [5] Shelke, Santosh. "Controllability of Radial Magnetic Bearing." *Procedia Technology* 23 (2016): 106-113.
- [6] Hamrock, Bernard J., Steven R. Schmid, and Bo O. Jacobson. *Fundamentals of fluid film lubrication.* CRC press, 2004.
- [7] Taylor, C. M., and D. Dowson. "Turbulent lubrication theory—application to design." *Journal of Lubrication Technology* 96.1 (1974): 36-46.
- [8] El-Shafei, A. and A. Dimitri, Controlling journal bearing instability using active magnetic bearings. *Journal of Engineering for Gas Turbines and Power*, 2010. 132(1)
- [9] Li, Qihang, et al. "Active rotordynamic stability control by use of a combined active magnetic bearing and hole pattern seal component for back-to-back centrifugal compressors." *Mechanism and Machine Theory* 127 (2018): 1-12.